Synthesis of sunlight responsive ternary G-C_3N_4/strontium ferrite/zeolite nanocomposite and investigation of its synergistic photocatalytic activity

Z. Waheed [a], N. Tahir [a], K. A. ElAziz [b], S. Noreen [a], U. Latif [c], H. T. Ali [b], G. Mustafa [d], I. Shahid [e], M. Zahid [a,*]

[a] *Department of Chemistry, University of Agriculture, Faisalabad- 38040 Pakistan*

[b] *Department of Mechanical Engineering, College of Engineering, Taif University, Kingdom of Saudi Arabia*

[c] *Interdisciplinary Research Centre in Biomedical Materials, COMSATS University Islamabad, Lahore Campus, Lahore, 54600, Pakistan*

[d] *Department of Chemistry, University of Okara, Pakistan*

[e] *Environmental Science Center, Qatar University, P.O Box 2713, Doha, Qatar*

In this study, the synthesis of a novel ternary nanocomposite (g-C_3N_4/$SrFe_{12}O_{19}$/Zeolite) and its application photocatalytic degradation of Rhodamine B dye under sunlight. UV-visible spectroscopy, XRD, FTIR, SEM, and EDX were employed to characterize the ternary composite. Maximum photocatalytic degradation of 94% was achieved under optimized parameters as pH 4, catalyst dosage 50 mg, oxidant dose 15mM, dye conc. 10 ppm and 90 minutes. Kinetics, catalyst reusability and radical scavenging investigations were carried out for dye degradation. The data was statistically evaluated using Response Surface Methodology. Toxicity analysis was performed to check the toxicity of treated wastewater to assure water quality.

(Received August 10, 2025; Accepted November 6, 2025)

Keywords: Heterogeneous photocatalysis, Strontium ferrite, Graphitic carbon nitride, Photo-fenton, Coal fly ash-based zeolite, Rhodamine B, Toxicity analysis

1. Introduction

The release of wastewater from chemical plants is a major contributor to degradation of the environment. The dyeing business is a significant contributor to water contamination, which poses serious risks to human and ecological health [1]. The fast industrialization and broad adoption of new technologies over the past two decades have led to a remarkable increase in organic pollutants in the environment [2]. Common contaminants include organic synthetic dyes, the yearly global output of which can reach 0.7 million tons [3]. The global production of organic dyestuff by various industries, including textiles, food, cosmetics, hair colour, leather, and electronics, amounts to approximately 0.28 million tons. [4].

Today, one of the main factors contributing to environmental deterioration worldwide is dye pollution. These are being poured straight into the water supply without any kind of purifying procedure, resulting in dirty, toxic, and discoloured water. [5]. The textile industry releases immense volumes of effluent containing dangerous chemicals during the dying process [6]. The dye reduces the amount of oxygen in the water, making it poisonous to plants, animals, and humans. The organic dyes' robust resistance to breakdown can be attributed to their complex structures, which provide them excellent biological, chemical, and photocatalytic stability [7]. Both human and environmental health are negatively impacted when excess dyes are released. For instance, the cationic xanthene dye rhodamine B (RhB) has found extensive use in the printing, textile, and photographic industries [8].

Dyes are carcinogenic, thus even trace amounts in water can hurt ecosystems [9, 10]. Dye removal from wastewater must be an efficient, straightforward, and inexpensive process. These

* Corresponding author zahid595@gmial.com
https://doi.org/10.15251/JOR.2025.216.705

conventional approaches typically suffer from issues including low efficiency, complexity, high operational expense, and limited scalability [11]. Physical, chemical, electrochemical, and biological processes are typically the focus of research into dye degradation methods. Physical procedures such as adsorption, irradiation, and ion exchange are no longer used. Current chemical processes can be broken down into subcategories including ozonation, advanced oxidation, and the Fenton process. There are other biological processes used, such as aerobic and anaerobic decomposition, fungi, and algae. Based on its effectiveness in eliminating color molecules, the advanced oxidation process (AOP) stands out as the most promising of these techniques [12].

A semiconductor photocatalyst is employed to get rid of these contaminants. The organic and inorganic materials are adsorbed onto the photocatalytic surface of the semiconductor, which undergoes a redox reaction in response to the illumination [13-15]. The photo-Fenton reaction includes photochemical reformation of Fe^{2+} via photo-reduction of ferric Fe^{3+}. The newly formed Fe^{2+} reacts with H_2O_2 to make •OH and Fe^{3+}, which continues the cycle. The direct H_2O_2 photolysis generates •OH that is used to degrade organic molecules, hence speeding up the degradation of organic contaminants. Photo-Fenton is better at degrading less concentrated organic contaminants because high levels of pollutants decrease the iron complex's ability to absorb radiation, which requires a longer irradiation period and a higher H_2O_2 dose. $SrFe_{12}O_{19}$ nanoparticles are used as heterogeneous catalysts for Fenton-like processes due to their strong catalytic activity. These nanoparticles catalyze H_2O_2 through intrinsic peroxidase-like activities to form hydroxyl radicals for degrading organic contaminants, while a considerable portion of them stay in the solid phase in the solution and can be reused [16]. In 2006, graphitic carbon nitride (g-C_3N_4) was first used as a photocatalyst [17]. There has been a significant increase in the interest in this subject matter within the photocatalysis community in recent years. Its bandgap is moderate and its visible-light sensitivity is satisfactory; its building blocks are tri-s-triazine units [18]. Composite materials enhance the properties (magnetic, optical, optoelectronic, etc) of constituent components, thus showing synergetic properties [19-21].

Coal fly ash or CFA is produced as a byproduct of coal-fired power generation. Research on techniques of recycling CFA is crucial, as the large amounts discharged annually pose serious risks to human and environmental health. The synthesis of zeolites is an efficient way to convert CFA into a marketable good, it has applications in areas as varied as farming, ecology, and business [22]. While zeolite and CFA have similar chemical make-ups, zeolite is distinguished by its distinct crystalline shape. However, CFA is characterized by its amorphous nature [23]. In addition, zeolite has more cation exchange capacity (CEC), a larger surface area, and enhanced thermal stability [24].

Wastewater treatment often employs inorganic adsorbents like zeolites, which are affordable microporous aluminosilicate minerals with the capacity to adsorb heavy metal ions and other hazardous chemicals from water sources [25]. The three-dimensional structures of natural zeolites consist of microporous SiO_4 and AlO_4 tetrahedra, and they are hydrated aluminosilicate minerals. The negative surface charge of zeolites means that they can only bind to cationic pollutants such as cationic dyes and heavy metal ions [26]. Because it slows down electron-hole recombination and helps delocalize electrons excited by band gap energy in semiconductors, it is an efficient catalyst in photodegradation [27]. Because of its benefits, we have selected zeolite as a support for g-C_3N_4 so that its photocatalytic activity and stability can be enhanced [28].

The use of magnetic nanoparticles for water purification has gained popularity in recent years [29]. Because of how compact they are and how well is their surface area to volume ratio, they have a high elimination capacity, fast kinetics, and substantial responsiveness towards pollutant removal. The improved magnetic properties of the catalyst are a bonus, allowing for its easy removal from water after the pollutant has been neutralised. Predictions indicate that magnetic separation will be more economically viable and operationally feasible than membrane filtration [30].

Hexagonal ($MFe_{12}O_{19}$), spinel (MFe_2O_4), and garnet ($M_3Fe_5O_{12}$) are only a few of the most prevalent crystal forms found in ferrites [31]. However, it's important to remember that M-type hexagonal ferrite—which comprises strontium hexaferrite ($SrFe_{12}O_{19}$), barium ferrite ($BaFe_{12}O_{19}$), and plumbum ferrite ($PbFe_{12}O_{19}$)—is the basic hard magnetic material [32]. M-type hexagonal ferrites are distinguished by elevated saturation magnetisation, significant coercivity and substantial uniaxial magnetic anisotropy [33]. Powdered Strontium ferrite is used across a diverse array of applications, from medicinal and biological instrumentation to print screens and base materials for

programmable filters, phase changers, detectors, generators, magnetic recording media, and even recorders and telephones [34].

Because of their appealing magnetic properties, include elevated saturation magnetisation, significant magneto-crystalline anisotropy, and high coercivity, low price and chemical stability, $SrFe_{12}O_{19}$ have earned a significant role in technical applications and fundamental research endeavours [35].

In this study, we synthesized a Ultraviolet responsive ternary nanocomposite and according to our comprehensive literature review, this nanocomposite has not been previously documented. To evaluate the photodegradation efficiency of ternary g-C_3N_4/Zeolite/$SrFe_{12}O_{19}$ (GSZ) nanocomposite, the Rhodamine B (RhB) dye was degraded using it. The catalyst was synthesized using hydrothermal synthesis, in which the individual components were initially prepared separately. The structure, composition, morphology, optical, and surface properties of the catalysts were examined using a variety of analytical techniques. The photocatalytic activity of ternary heterojunction was compared with binary g-C_3N_4/$SrFe_{12}O_{19}$ (GS) and g-C_3N_4/Zeolite (GZ) nanocomposites. The exceptional photocatalytic activities are the result of low recombination rates and high electron-hole separation efficiencies.

2. Experimental Section

2.1. Materials and reagents employed during experimental study

Fe $(NO_3)_3.9H_2O$, Iron (III) Nitrate Nonahydrate, 98% and Strontium Nitrate ($(SrNO_3)_2$, 97%) were purchased from Duksan Reagents. Melamine ($C_3H_6N_6$, 99%) was purchased from DAEJUNG. South African Fly Ash obtained from coal was used. Hydrochloric acid (HCl) and sodium hydroxide pellets were bought from Sigma Aldrich. Hydrogen peroxide (H_2O_2) and ethylene glycol were acquired from the reagent company UNI-CHEM. Ethanol (C_2H_5OH, 95.6%) was procured from the Merck firm. The model pollutant for photodegradation study was Rhodamine B (RhB), a cationic dye obtained from Sigma Aldrich. Throughout the synthesis process, distilled water was acquired from a water a local distillation plant and employed for the formulation of reaction solutions.

2.2. Synthesis of binary g-C_3N_4/Zeolite (GZ) nanocomposite

25 millilitres of ethylene glycol were combined with half a gram of graphitic carbon nitride and half a gram of zeolite using ultrasound for two hours. The mixture was thereafter heated to 120 degrees Celsius in a stainless steel autoclave lined with Teflon for eight hours. The next step was to bring the autoclave down to room temperature. After removing it from the autoclave, the product was rinsed with water and then left to dry for eight hours at 60°C [27].

2.3. Synthesis of binary g-C_3N_4/ $SrFe_{12}O_{19}$ (GS) nanocomposite

In 60 mL of methyl alcohol, 0.5g of g-C_3N_4 was dispersed using ultrasonication for 30 minutes. 0.5g of $SrFe_{12}O_{19}$ was then carefully added to the mixture and the solvent was completely dried by refluxing strontium hexaferrite at 80°C with constant agitation. After drying in a vacuum at 60^o C for 24 hours, the resultant material was ground to a fine powder [36]

2.4. Synthesis of ternary g-C_3N_4/ $SrFe_{12}O_{19}$/Zeolite (GSZ) nanocomposite

The equal quantities of zeolite and g-C_3N_4 in 20 mL of water were sonicated separately for 15 minutes. Then both solutions were added while preparing $SrFe_{12}O_{19}$ one by one on stirring. Then, the Teflon-lined hydrothermal reactor was filled with this mixture and heated up at 180 degrees Celsius for 24 hours. To remove the precipitate from the solution, distilled water was utilised. After 24 hours of drying at 65°C, the final product was obtained. The schematic presentation of synthesis of all binary and ternary nanocomposites is described in Fig.1.

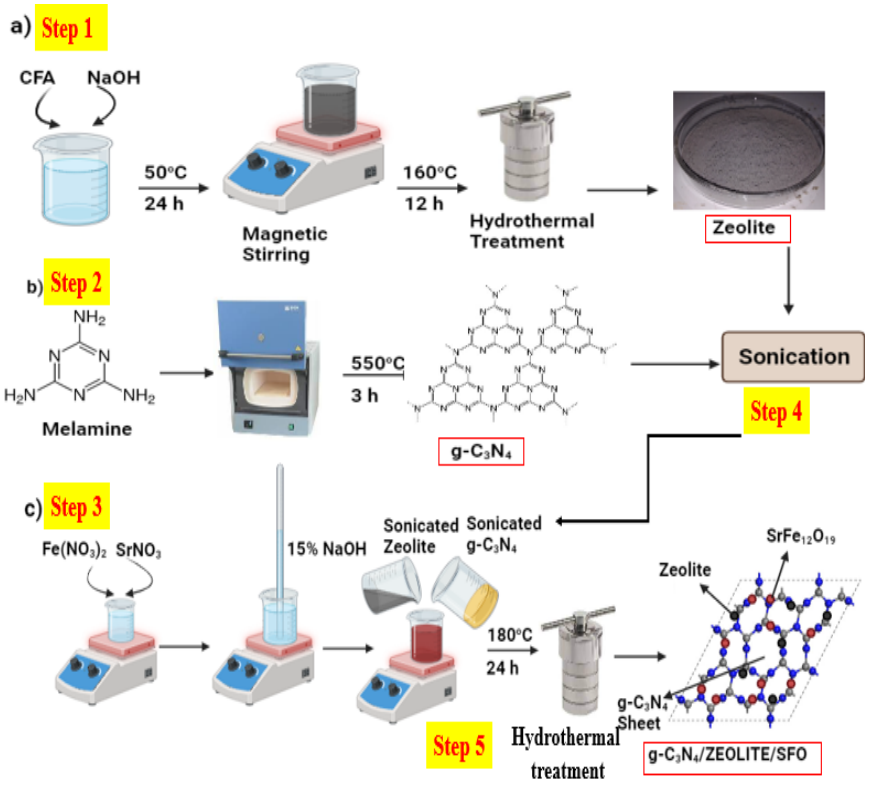

Fig. 1. Synthesis of Ternary nanocomposite g-C_3N_4/ $SrFe_{12}O_{19}$/Zeolite hydrothermally.

2.5. Characterization

To analyze the complete crystal structure of the synthesized binary and ternary photocatalysts, X-ray diffraction (XRD) was performed with a Bruker D8 Advance instrument with Cu-K radiation (= 1.540598) and a 2θ range of 10-80°. Using energy dispersive X-ray spectroscopy (EDX) and scanning electron microscopy (SEM, Carl Zeiss EVO 18), the surface morphologies of the g-C_3N_4, Zeolite, and $SrFe_{12}O_{19}$ nanocomposite were investigated. By distributing catalysts in water while applying ultrasonication, a UV-VIS spectrophotometer (Cecil CE 7200) was used to analyze the bandgap of the binary and ternary composites in the 200-800 nm region. Using a scanning electron microscope with EDX (SEM-EDX; FEI NOVA 450 NANOSEM), the microstructure, morphology, and elemental analysis of composites were characterized. Different functional groups of the photocatalysts was examined using FTIR, Thermo Nicolet.

2.6. Photocatalytic activity determination:

In this investigation, we chose to use Rhodamine B (RhB) dye as a representative contaminant. 10 ppm of dye solution was used in the degradation. To get to the target pH, 0.1 M NaOH and HCI solutions were each utilised. To enhance the interactions between the catalyst and dye molecules, we ultrasonicated the dye solution for 1 minute following the addition of the finely powdered catalyst. All of the trials took place in ambient conditions.. After the reaction mixture was sonicated, it was subjected to ultraviolet light for a specific duration while being shaken at a speed of approximately 150 rpm in an orbital shaker (Pamico Technologies). When the catalyst was taken out of the reaction mixture, the absorbance at 546 nm was measured with a UV-visible spectrophotometer (CECIL CE 7200). We were able to ascertain the dye solution's degradation percentage by comparing the absorbance of treated and untreated solutions.

$$\% \text{ Degradation} = 1 - \frac{A}{Ao} \times 100 \quad (1)$$

2.7. Response surface methodology (RSM)

The effectiveness of photocatalysts is affected not only by the amount of catalyst present, but also by the pH, oxidant dose, reaction time, and concentration of the dye. Here, RSM is demonstrated as an efficient way for optimizing processes involving multiple, interrelated variables. Reduced experimental errors and improved data fitness are the outcomes of using the Box Behnken design (BBD) in process design, modeling, and optimization rather than the central composite design (CCD) to estimate the correlation coefficient (R^2) for a given model.

3. Detailed results and structural analysis discussion

3.1. FTIR analysis

The 807 cm^{-1} absorption peak for pure g-C_3N_4 is due to the triazine ring's characteristic out-of-plane bending modes [37]. The 1200–1650 cm^{-1} absorption bands were found to correspond to the usual stretching vibration of C–N heterocycles. The aromatic C-N stretching vibration mode was attributed to the peaks at 1231, 1327, 1417, and 1573 cm^{-1}, whereas the C=N stretching vibration mode was attributed to the peak at 1643 cm^{-1} [38]. N-H bond stretches from -NH_2 and O-H, possibly due to moisture adsorption, producing a wide band at 3000-3400 cm^{-1} [39]. The zeolite's Al-O-Al and A-O stretching vibrations shield the Si-O-Si asymmetric stretching vibration, which is responsible for the strongest and broadest absorption bands between 930 and 1085 cm^{-1} [40]. The FT-IR spectra of a g-C_3N_4 /zeolite composite show that both zeolite and g-C_3N_4 have prominent distinctive peaks. In comparison to pure zeolite, the zeolite/g-C_3N_4 nanocomposite exhibited a little change in the positions of the key characteristic peaks Si-O and Al-O stretching vibrations. These changes indicate that the zeolite and g-C_3N_4 counterparts have successfully formed intimate interfacial contact. Interestingly, zeolite loading resulted in a diminution of the peak intensities of g-C_3N_4 with only minor changes. In this way, the created heterojunction structure is in favour of the separation of photogenerated charge carriers, which has a synergistic impact on boosting the photocatalytic activity [27]. Metal-oxygen bond peaks, at 611, 555, and 449 cm^{-1}, may be seen in the spectra of pure $SrFe_{12}O_{19}$ NPs. The hexaferrite structure's vibrations give rise to $SrFe_{12}O_{19}$ unique metal-oxygen peaks. In the octahedral site, the peak at 449 cm^{-1} may be associated with Fe-O bending vibration, whereas the higher frequency band at 611 cm^{-1} may be related to Fe-O stretching vibration in the tetrahedral site. The weaker peak at 555 cm^{-1} may perhaps be associated with a bending vibration in the Sr-O molecule. The detail of Transmittance peaks related to various functional groups are explained in Fig. 2.

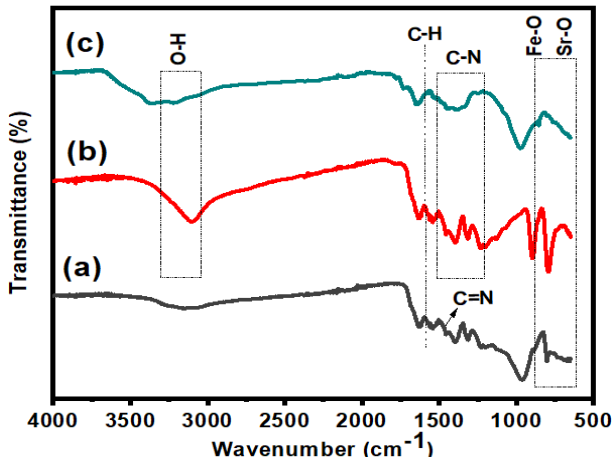

Fig. 2. FTIR Spectrum of binary (a) CZ (b) GS and ternary (c) CGS.

3.2. XRD analysis

The various diffraction peaks of ternary and binary nanocomposites are shown in Fig. 3. $SrFe_{12}O_{19}$ exhibits diffraction peaks at 18.8°, 30.3°, 32.4°, 35.5°, 40.4°, 42.5°, 47.3°, 50.2°, 53.1°, 56.2°, 60.2°, and 63.04°, which can be attributed to the reflection of (006), (110), (106), (107), (114), (203), (205), (206), (301), (217), (218), (304), and (307), reveals the pure crystalline form of $SrFe_{12}O_{19}$ with hexagonal structure (JCPDS No. 33–1340). The diffraction peaks of $SrFe_{12}O_{19}$ closely related to micro-spherical morphology have well-defined and sharp peaks in all composites, signifying successful formation of $SrFe_{12}O_{19}$. The g-C_3N_4 diffraction peaks observed at 13.1° and 27.4° are associated with indexes (100) and (002). Major peaks in the XRD pattern of Zeolite can be seen at 23.28°, 27.45° and 30.03°, and 45.2° which all correlate to the (533), (642), (733), and (555) reflection planes. The strong peaks at 23.28° and 30.3° are associated to the prominent CFA composition related to quartz and a relatively less intense peak (45.2) of zeolite are related to hematite, in accordance with the previous studies [41]. Due to the low diffraction intensity of g-C_3N_4, the matching diffraction peak was barely apparent in the XRD pattern after being hybridized with semiconducting materials. Crystals favors the (100) orientation, as demonstrated by the tiny peak intensity of the reflection from the (100) plane in g-C_3N_4. Due to the strong crystalline character of the binary nanocomposite and deposition of strontium ferrite in support, its peaks are noticed with reduced intensity compared to ternary GSZ peaks [42]. Debye-Scherrer's equation can be used to determine the crystallite size.

$$D = K\lambda/\beta\cos\theta \tag{2}$$

K=shape factor=0.94, λ=wavelength of X-ray radiation in Cu k1 (= 1.5406 Å), β=Full-Width Half Maximum (FWHM) intensity, θ=Bragg's angle. The particle sizes of GZ, GS, and GSZ are calculated to be 132 nm, 129 nm, and 111 nm respectively.

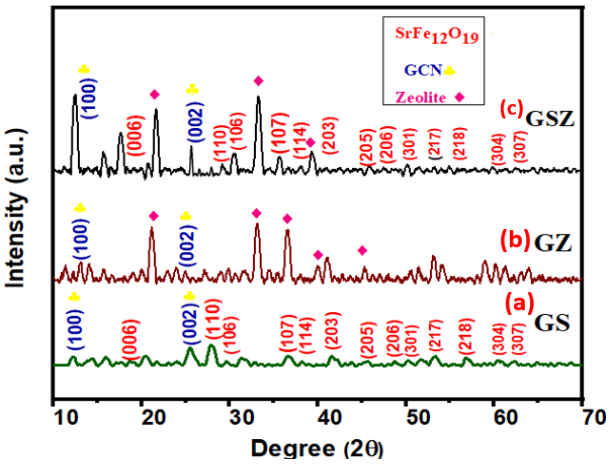

Fig. 3. XRD pattern of (a) GS (b) GZ and (c) GSZ nanocomposites.

3.3. SEM-EDX analysis

Scanning electron micrographs of binary and ternary nanocomposites are shown in Fig. 4. The $SrFe_{12}O_{19}$ nanoparticles showed micro-spherical morphology which is clearly shown in inset Fig 4(e). All the $SrFe_{12}O_{19}$ microspheres are nearly homogenous in shape and size [43]. The zeolites are clear microneedle structures, typically between three and five micrometers long as confirmed by the previous literature [41] It is evident from scanning electron micrographs of the g-C_3N_4/Zeolite nanocomposite that the CFA based Zeolites microneedles were immobilized onto the relatively smooth surfaces of the g-C_3N_4 matrix Fig. 4 [44]. In ternary nanocomposite, g-C_3N_4 is a sheet with a wrinkled interplanar structure. The energy dispersive X-ray (EDX) spectroscopy picture indicates that the manufactured material comprises C and N elements and that no impurity element peaks

were seen, this validates the purity of the g-C_3N_4 [45]. The EDX spectrum clearly shows the six most abundant elements carbon, nitrogen, oxygen, sodium, Aluminium, and silicon. The EDX spectrum found that carbon, nitrogen, sodium, Aluminium, silicon, and oxygen were all present in varying quantities. No other element peak was seen in the EDX analysis, indicating the purity of the synthesized compounds [27]. The elements Sr, Fe, and O, which make up strontium hexaferrite, have been confirmed by EDS analysis [46].

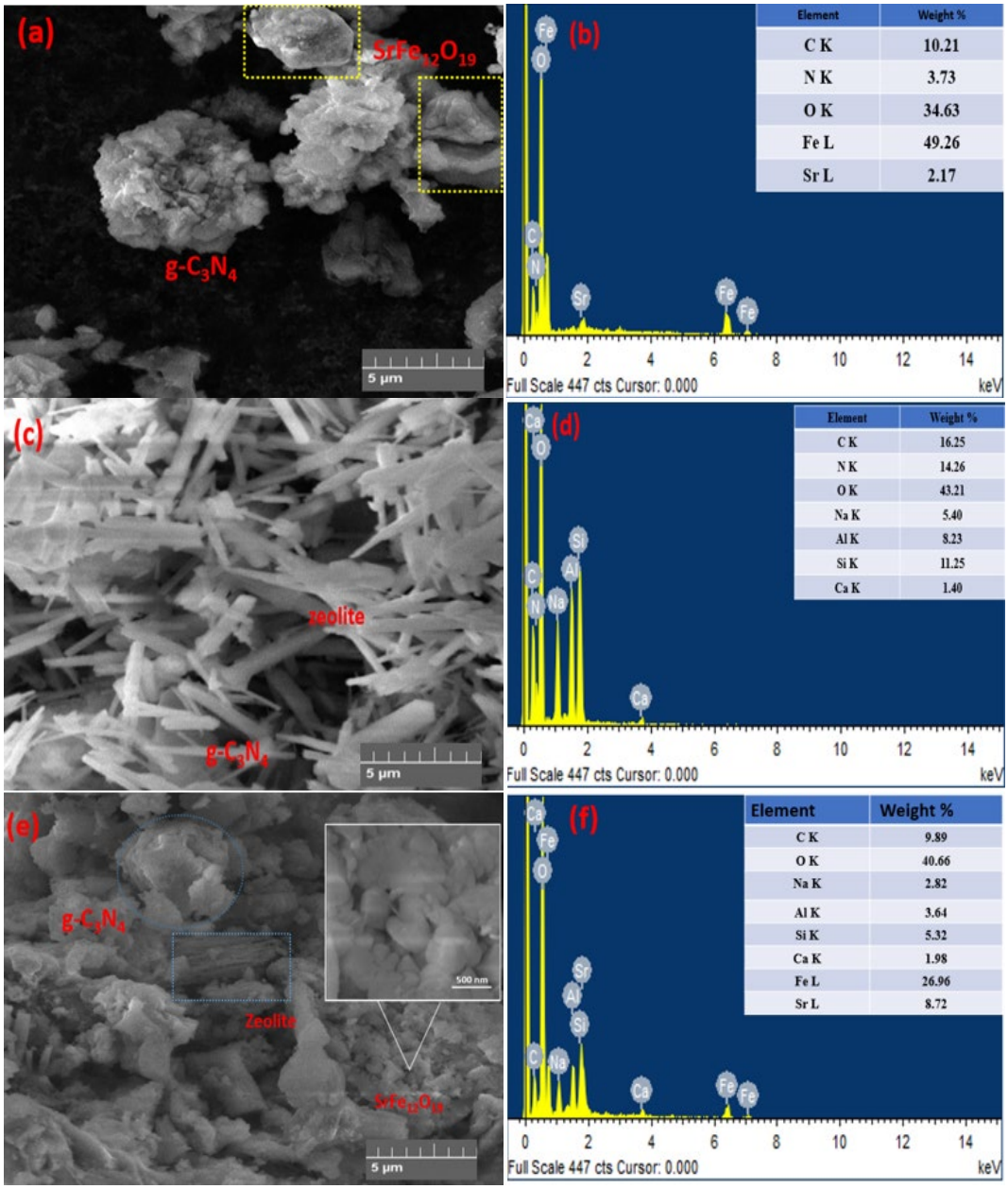

Fig. 4. SEM-EDS images of binary (a & b) GS (c & d) GZ and ternary (e & f) GSZ.

4. Optimization of parameters for RhB degradation

4.1. Point of zero charge determination

A solution of 0.01 M sodium chloride was made in order to determine the point zero charge. On a hotplate, the solution that had been made was put so that CO_2 could be removed. Following the appearance of bubbles, the beaker that held the solution was taken off of the hotplate and set

aside. The pH of the NaCl solution was adjusted to the values of 2, 4, 6, 8, and 10 with the help of a 0.1M solution of HCL, as well as NaOH. After that, composite in the ratio of 75 mg/50 mL was added to each beaker after the pH had been adjusted. After covering the beakers with aluminum foil, they were put on an orbital shaker in the ultraviolet chamber for a period of twenty-four hours. The ultimate pH was determined after 24 hours had passed. The surface charge of the composite was found to be proportional to the difference between the initial and final pH levels. Results depicted the point zero charge on GSZ was 3.3 (Fig.5).

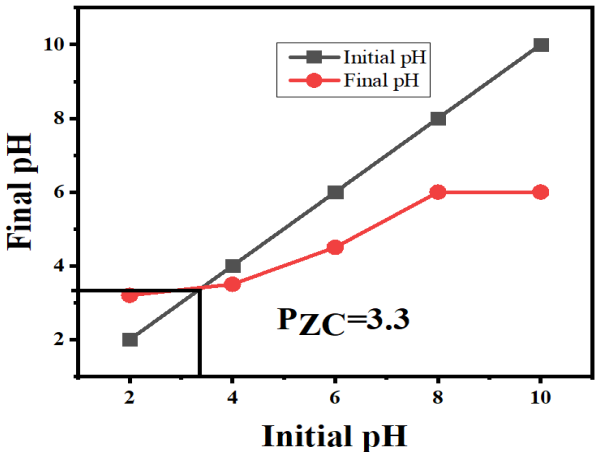

Fig. 5. Point zero charge of GSZ ternary nanocomposite.

4.1. Effect of pH

The pH of the dye solution had a substantial impact on the rate of photodegradation. Therefore, solutions of RhB dye were tested for their photodegradation at a range of pH values (from 2 to 9) using 0.1M HCl and NaOH. After adjusting the dye solution's pH, we added 50 mg/50 mL of g-C_3N_4/SFO/ZEOLITE, 20 mg/50 mL of g-C_3N_4/Zeolite, and 20mg/50 mL of g-C_3N_4/SFO, respectively, and sonicated the mixtures. Then, H_2O_2 was introduced as an oxidant. The proportion of deterioration was determined by repeatedly taking samples at regular intervals. Dye was degraded by a ternary composite most effectively (94% effective) at a pH of 4, Fig. 6(a). The results indicates the photodegradation of RhB dye solutions using the g-C_3N_4/Zeolite composite was greater (83%) when the pH is neutral or basic rather than acidic. Because the p_{ZC} of g-C_3N_4/zeolite composite is close to 7. At pH 4, the maximum degradation rate was found, and 87% of RhB was destroyed in 90 minutes via photocatalytic degradation using g-C_3N_4/SFO.

4.2. Effect of catalyst dose

The effect of the catalyst dose is shown in Fig. 6(b). By changing the amount of catalyst used from 10 mg to 100 mg while maintaining all other parameters at the same value, the effect of catalyst dose on RhB degradation was studied. Increasing the catalyst weight from 10 mg to 100 mg boosted the rate of photodegradation efficiency, however, after that, the efficiency of degradation declined. When dosed more heavily, particles agglomerate and the screening effect becomes more pronounced, limiting ROS production. RhB was photocatalytically degraded to 93% for GSZ ternary composite at 50 mg/50 mL, 84% and 87% for GZ and GS composites at 20 mg/50 mL.

4.3. Effect oxidant dose

Experimental settings were used for H_2O_2 process optimization: RhB concentration=10 ppm, pH=4, and catalysts dose=50 mg/50 mL are optimal conditions for the GSZ composite. Dye degradation was shown to increase linearly with increasing oxidant concentration from 10 to 40 mM. This establishes the ideal oxidant dosage for producing an adequate amount of OH. In order to finish the oxidative catalytic destruction of contaminants, the ternary composite required 15 mM of

radicals, while the two binary composites only needed 10 mM. Dye degradation slowed with increasing oxidant concentration, possibly because of the scavenging effect of the hydroxyl radical and related processes [47], as shown in Fig. 6 (c).

4.4. Effect of initial dye concentration

As rhodamine B concentrations were increased, degradation rates were shown to decrease. After 90 minutes of exposure to sunlight, GSZ degraded 10, 20, 30, and 40 ppm of rhodamine B to 94%, 87%, 75%, and 66%, respectively. The photocatalyst's surface is coated with RhB molecules, at lower concentration (10 ppm), would undergo surface interaction with hydroxyl (OH•) radical produced on the catalyst surface. With enough hydroxyl radicals produced, RhB would be successfully degraded. RhB solution acts as a shield, preventing light from reaching the catalyst and causing insufficient photon interaction, electron-hole pair creation, and hydroxyl radical formation at high concentrations. In addition, a decrease in the proportion of photocatalytic degradation occurs at larger concentrations because molecules swarming over the catalyst surface may eventually block the active sites Fig. 6(d).

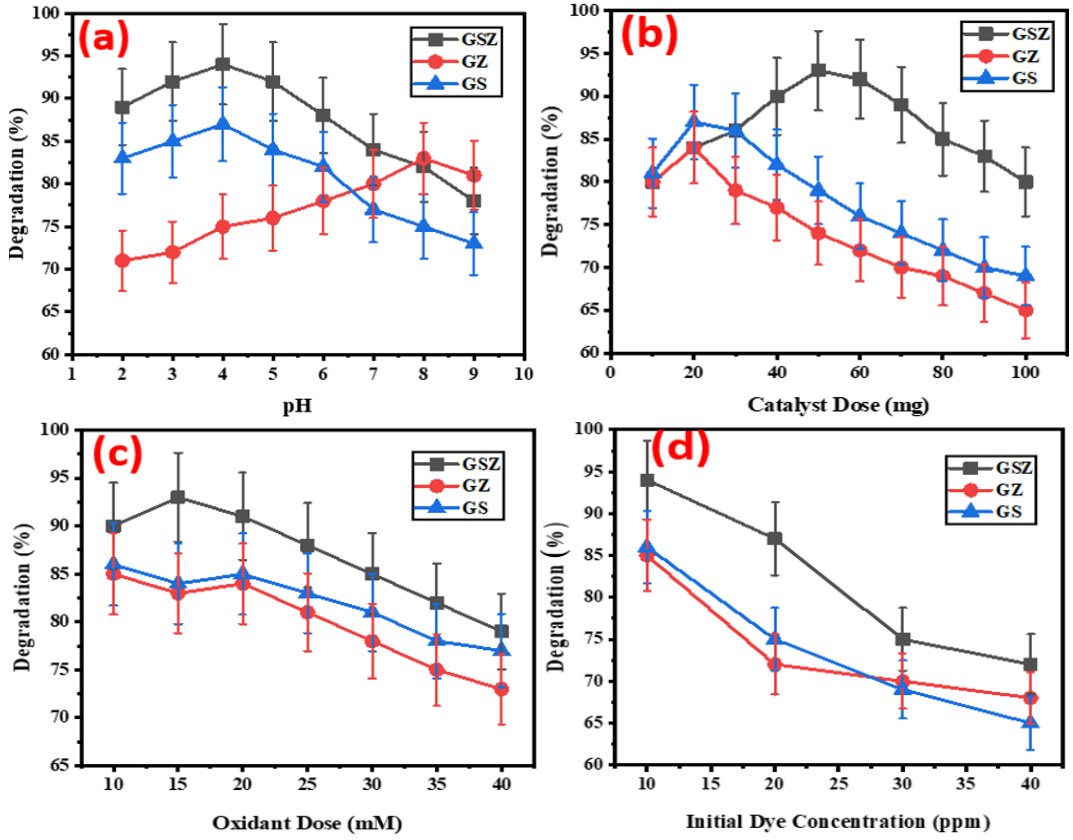

Fig. 6. Effect of (a) pH, (b) catalyst dose, (c) oxidant dose, (d) dye concentration, on RhB degradation.

4.5. Effect of time

Increases in reaction rate have a beneficial effect on dye degradation percentages because they bring the reaction closer to completion. The percentage of RhB degradation was measured at various times (10-90 min) under ideal conditions. Aliquots were obtained at regular intervals from the reaction mixture, and their degradation percentage was measured with a UV-visible spectrophotometer. At the 90-minute mark, the photocatalytic degradation of RhB reached its peak. Fig. 7 (a & b).

4.6. Reusability test and iron leaching analysis

The reusability of any catalyst is the most unique and important factor in determining the industrial utility of that catalyst. In order to ensure that photocatalysts are suitable for practical applications, it is essential to explore their stability. As a result, an experiment study on their recyclability was also conducted. The catalysts were recovered when the reaction was completed under optimal circumstances, rinsed multiple times with distilled water, reweighed, and reused. After five uses, a catalyst's recovery yield drops by a small amount, while the percentage deterioration drops from 96% to 86%. Fig. 7(c) demonstrates that the photocatalysts GSZ for the breakdown of RhB dye was stable for up to five cycles in a row. The recycling test results show that g-C_3N_4/$SrFe_{12}O_{19}$/Zeolite is highly resistant to dye degradation when exposed to sunlight. The slight decline in degradation efficiency after the third run-up to the fifth cycle was owing to the surface deposition of degraded catalyst particles [48].

Heterogeneous photocatalysts need to be resistant to metal leaching from the solid to liquid phase for their practical usage (in wastewater treatment). After five cycles, AAS was used to verify the iron leaching for all three catalysts. The AAS analysis guarantees that the catalysts are stable because it produces almost no iron leaching (~ 0.03 mg/L). In contrast to what was expected (2.0 mgL^{-1} by European Union directives), iron leaching was found to be significantly lower. Catalysts are eventually rendered ineffective due to the slow but steady leaching of trace metals. The drop in photocatalytic effectiveness with repeated usage may be attributable to a combination of blocked active sites and a decline in total active sites. The catalyst's structure and performance may shift as a result of these influences [49].

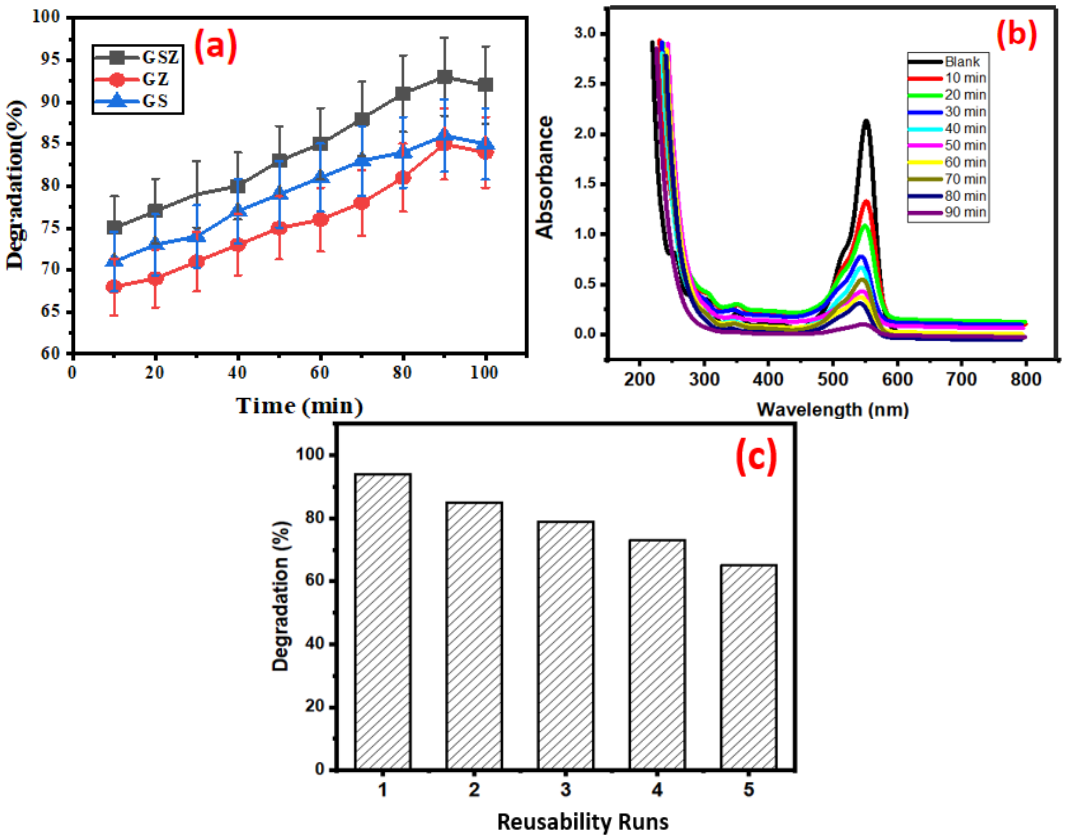

Fig. 7. (a) Effect of Time duration on RhB degradation by GSZ (b) UV-vis time scan of RhB degradation by GSZ (b) Reusability cycles by GSZ.

4.7. Toxicity analysis

Both primary and secondary treated wastewater are utilised by the irrigation systems that are used for horticulture, landscaping, and food crop production. Tertiary treatment of wastewater involves the use of advanced oxidation techniques to break down organic pollutants into carbon dioxide. As a result, surface groundwater might be replaced by the water. Considerations pertaining to the environment and society have led to the utilization of treated wastewater FOR the cultivation of food crops. The breakdown of pollutants in dye-loaded wastewater treatment using magnetic nanocomposites under ultraviolet light is an essential process. It all comes down to the quality of the byproducts. Applying Rhb dye water with GSZ nanocomposite to extremely delicate wheat seedlings allowed us to achieve our objective. After submerging the filter sheets and seeds in a 10-milliliter solution of treated RhB dye, the mixture was sealed with glass lids. For one day, the Petri dishes were left to incubate at room temperature. In just over a week, wheat seeds began to sprout (Fig. 8). RhB-treated wastewater was not darkened by the seeds. The treated water can now be safely used for agricultural irrigation. Therefore, under ideal conditions, treated water can be used for irrigation.

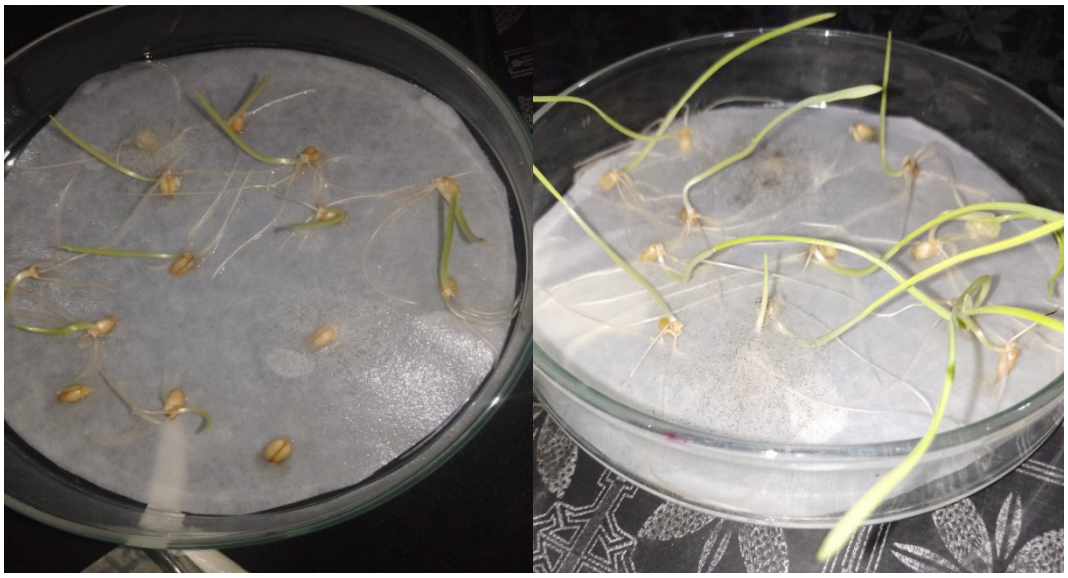

Fig. 8. Analyzing the RhB water's toxicity using ternary GSZ on wheat seed.

4.8. Radical scavenging experiment

Photocatalytic degradation is promoted by reactive species such as hydroxyl radicals, electrons, and holes. Therefore, employing radical scavenging species, it is possible to check the effectiveness of the radicals responsible for degradation. Potassium dichromate ($K_2Cr_2O_7$) for electron, as well as dimethyl sulfoxide (DMSO) for Hydroxyl radical, radical scavengers like EDTA and DMSO were utilized for holes. In the context of photocatalysis, it is common to think of holes (h^+), hydroxyl radicals (OH), and superoxide ion radicals ($O_2^{\cdot-}$) as the reactive species [50].

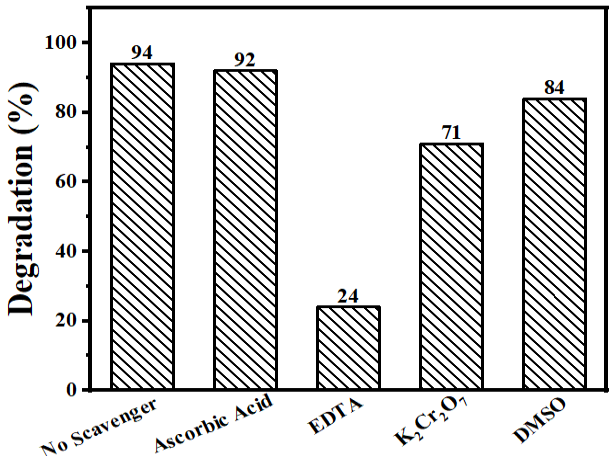

Fig. 9. Radical scavenging experiment for dye degradation by ternary GSZ.

The primary reactive species responsible for the reactions in the photocatalytic system were isolated through a series of studies in which scavengers were added to the reaction system. Under all optimized conditions, four beakers were taken and 5mM of the each scavenger was added to each. The outcome demonstrates that utilizing Ascorbic Acid and DMSO significantly reduce the rate of dye solution degradation. Degradation was decreased from 96 to 24 percent. Similarly, the deterioration was lessened by the participation of electron and holes scavengers (Fig. 9).

4.9. Proposed mechanism

Photodegradation of dye relies heavily on holes and hydroxyl radicals, as stated in the hypothesized mechanism. To the best of our knowledge, the formation of the h^+ and e^- involved in the degradation process requires the light energy in excess of the bandgap energy. Light striking the surface of the GSZ composite rapidly stimulates electrons from the valence band (VB) toward the conduction band (CB) because of the combination of SFO with GCN, which lowers the bandgap of GCN via easy charge transfer. The photoexcited electrons leave the VB of SFO and move towards the CB of GCN. It takes more time for recombination to occur in GCN because holes move closer to the VB of zeolite. These photogenerated holes lowered the H_2O_2, leading to the formation of the superoxide radical.

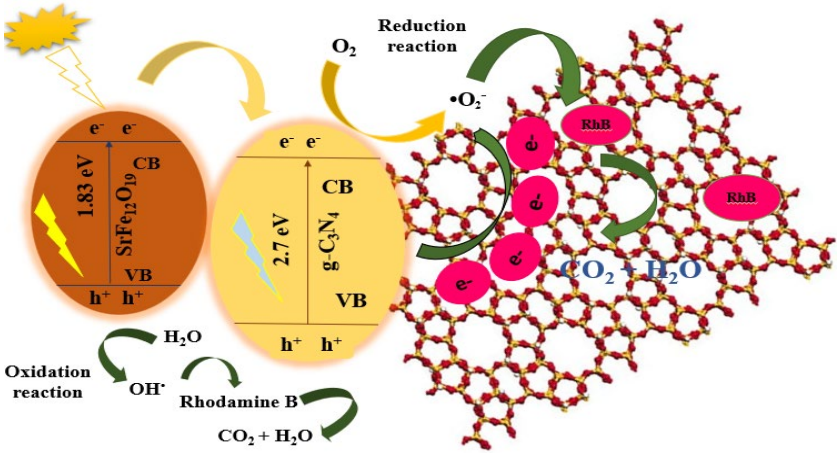

Fig. 10. Proposed mechanism for the degradation of the RhB dye by means of ternary GSZ.

The proposed RhB degradation mechanism by ternary GSZ is shown in Fig. 10. At first, the molecules of RhB were adsorbed onto the composite's surface. After being exposed to sunlight, the composite material undergoes charge separation, with e^- in VB being stimulated to CB and h^+ being

simultaneously generated in the VB. H_2O_2 could successfully capture the photo-generated electrons, resulting in $OH^{\cdot}$ radicals. In the meantime, the Fe^{3+} can act as a trap for electrons, transforming them into Fe^{2+} so that they can participate in the Fenton reaction and generate even more hydroxyl ($OH^{\cdot}$) radicals [51]. The photo-Fenton process can greatly enhance the oxidation capacity of Fenton mixtures. The $OH^{\cdot}$radicals degraded the adsorbed RhB molecules by giving carbon dioxide and water.

$$\text{Catalyst} + h\nu \rightarrow \text{Catalyst}\,(h^+ + e^-)$$
$$H_2O_2 + e^- \rightarrow {}^{\cdot}OH + OH^-$$
$$Fe^{3+} + e^- \rightarrow Fe^{2+}$$
$$Fe^{2+} + H_2O_2 \rightarrow Fe^{3+} + {}^{\cdot}OH + OH^-$$
$$Fe^{3+} + h\nu + OH^- \rightarrow Fe^{2+} + {}^{\cdot}OH$$
$$h^+ + H_2O \rightarrow H^+ + {}^{\cdot}OH$$
$$h^+ + OH^- \rightarrow {}^{\cdot}OH$$
$${}^{\cdot}OH + RhB \rightarrow CO_2 + H_2O$$

4.10. Kinetic models for rhodamine B degradation by ternary GSZ nanocomposite

The heterogeneous Fenton process shows multiple reactions hence kinetic study is more complicated. Usually, pseudo-first-order kinetics models were used for photocatalytic degradation of organic compounds. So a model is described in which degradation of Rhodamine B is described to explain experiment work. To find optimal results in absolute use, the number of mathematical models was consequent in the present research work.

Using pseudo 1st and 1st order kinetic models to the experiments allowed for the analysis of the kinetics of RhB dye degradation.

Below are the equations for such models.

$$\ln C_t = K_1\, t \qquad \text{(Pseudo First order)}$$
$$\ln C_o/C_t = K_2\, t \qquad \text{(First order)}$$

Here, C_o denotes the dye solution's initial concentration at time zero and C_t at the specific time indicated by t. The pseudo-first and first-order reaction rate constants are denoted by the K_1 and K_2. Linear regression of the C_o/C_t against the time graph yields a slope equal to the apparent first-order rate constant K_1. For the first-order reaction of GSZ, the higher rate constant K_2 is more efficient than K_1 under sunlight. Fig. 11 shows that all binary and ternary nanocomposites effectively follow Pseudo first order model.

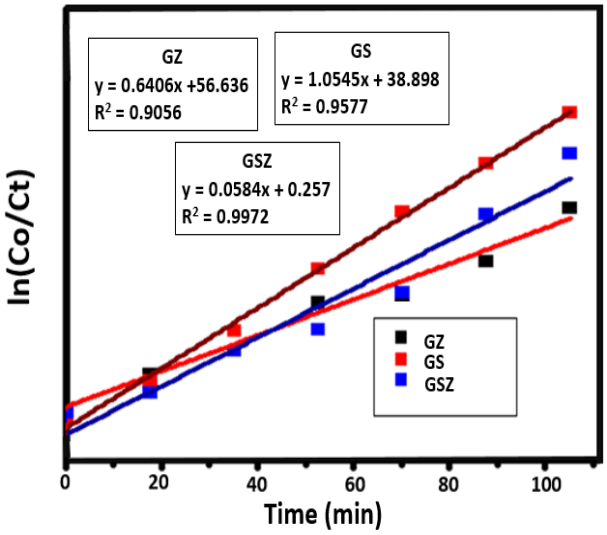

Fig. 11. Pseudo first-order fitting of binary and ternary nanocomposites.

Table 1. Kinetic modelling of RhB degradation by GSZ nanocomposite.

UV- Visible light responsive nanocomposites	Adjusted batch experiments conditions			Psuedo First-order kinetics		PseudoSecond-order kinetics	
	pH	dose(mg/ 100mL)	H_2O_2 dose (mM)	k1(min^1)	R^2	K2 ($L\mu mol^1$ min^1)	R^2
GZ	4	50 mg	15 mM	0.08	0.90562	0.521	0.8075
GS	4	20 mg	10 mM	0.06	0.9577	0.345	0.6551
GSZ	4	20 mg	10 mM	0.6	0.9972	0.1578	0.6345

4.11. Response Surface Methodology (RSM)

A notable way for improving a variety of components concerned in the photo-catalytic degradation process is the response surface methodology central composite designing methodology was employed as part of this inquiry to look at how different properties affected how quickly RhB deteriorated. To achieve the best possible percentage of degradation, the use of BBD made it possible to control separate elements including pH, catalyst dose, and time

4.11.1. Analysis of variance (ANOVA)

It is abundantly obvious from the fit result plot that the models that was used has a significant influence on the values that were optimized. The excellent R^2 value further demonstrates the model's strong predictive ability. Using a quadratic model, it was found that there is a strong correlation between the degree of deterioration and variables such pH, catalyst amount, and time. In order to determine how the aforementioned elements affected much of the RhB dye was destroyed, it made use of a 2nd order polynomial equation. This equation can be expressed as follows:

$$Y = \beta_\circ + \sum_{i=1}^{k} \beta_i x_i + \sum_{i=1}^{k} \beta_{ii} x_i^2 + \sum_{i=1}^{k} \sum_{i \neq j=1}^{k} \beta_{ij} x_i x_j + \in \quad (4)$$

The appropriateness of a model for a given set of data is determined via regression analysis and the existence of fit. The p-value reveals whether or not a given variable is statistically significant. When $p>0.1000$, the model is no longer statistically significant, while $p<0.05$ indicates a significant finding. If p-value<0.0001, the model is statistically significant.

Y stands for the response of the dependent variable (% degradation), $\beta\_\circ$ stands for a coefficient with a specific value, β_i stands for a linear coefficient, β_ii stands for a quadratic coefficient, and β_ij stands for the value of a coefficient representing interaction effects. Independent variable codes are denoted by x_i and $x\_\ j$, while random error $\in$ is denoted by 7.

$$Y=+92.13-2.74*A-0.2696*B-0.5625*C+0.2500*AB+0.2500*AC+1.50*BC-6.47*A^2-0.9925*B^2-1.35C^2 \quad (5)$$

For a given level of each coded factor, the reaction may be predicted using the corresponding equation. By default, a high level of a factor is designated as 1, while a low level is designated as -1. The encoded equation allows for the determination of the relative relevance of elements by comparing their coefficients.

Table 2. ANOVA table for RhB dye degradation by ternary GSZ nanocomposite.

Source	Sum of Squares	Df	Mean Square	F-value	p-value	
Model	733.29	9	81.48	35.02	<0.0001	Significant
A-Ph	102.72	1	102.72	44.16	<0.0001	
B-Catalyst Dose	0.0074	1	0.0074	0.0032	0.9561	
C-Oxidant Dose	0.0074	1	0.0074	0.0032	0.9561	
AB	0.5000	1	0.5000	0.2149	0.6529	
AC	0.5000	1	0.5000	0.2149	0.6529	
BC	8.00	1	8.00	3.44	0.0934	
A^2	621.75	1	621.38	267.11	< 0.0001	
B^2	7.74	1	7.74	3.33	0.0982	
C^2	7.74	1	7.74	3.33	0.0982	
Residual	23.26	10	2.33			
Lack of Fit	6.43	5	1.29	0.3820	0.8428	Not significant
Pure Error	16.83	5	3.37			
Cor Total	756.55	19				

Std. Dev.	1.53	**R^2**	0.9693
Mean	86.65	**Adjusted R^2**	0.9416
C.V. %	1.76	**Predicted R^2**	0.9036
		Adeq Precision	21.4874

The percentage of dye that has been degraded is denoted by Y, while the variables pH, catalyst concentration, and oxidant dose are shown by A, B, and C, respectively. AB, AC, and BC reflect linear relationships between independent variables, whereas A^2, B^2, and C^2 stand for quadratic effects.

A three-dimensional model in addition to a contour plot are used to illustrate the connection between the two parameters (Fig. 12). Catalyst concentrations ranging from 30 to 50 mg/100 mL and pH values between 2 and 6 were used for the investigation. Increasing the concentration of the catalyst causes the nanoparticles to aggregate, which in turn blocks the active sites. This means that the photocatalyst's degradation rate will slow down when it is exposed to sunshine.

The oxidant doses ranged from 10 mM to 40 mM. The photocatalytic activity was enhanced by a rise in oxidant concentration from 10 to 40 mM. Maximum degradation was achieved at 15 mM, and then there were no noticeable alterations after that.The trials employed catalyst concentrations ranging from 10 mg to 50 mg in 50 mL and oxidant doses ranging from 10 mM to 40 mM. Maximum degradation occurred at concentrations of 50 mg/50 mL and time of 90 minutes.

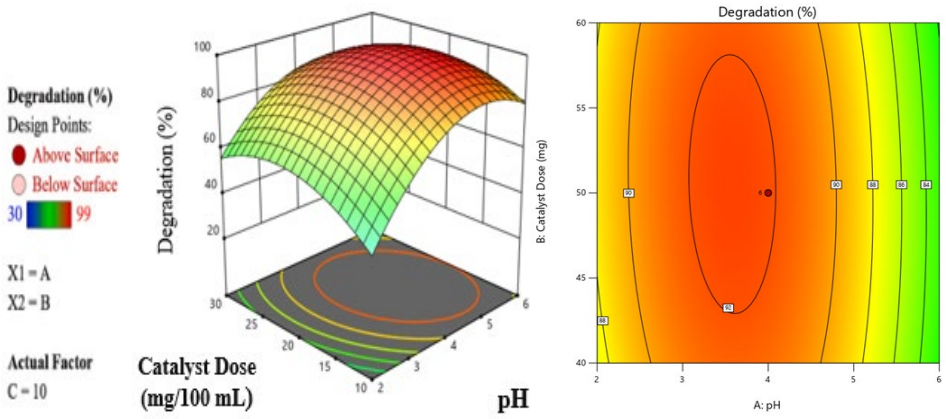

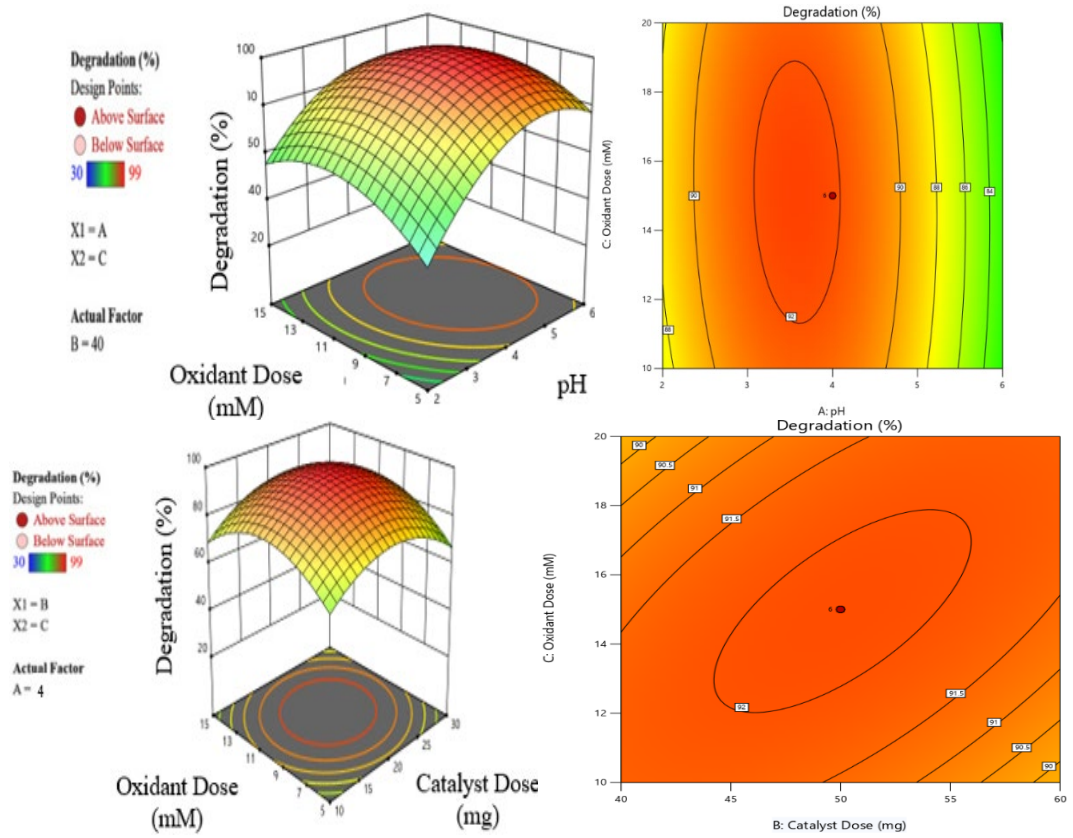

Fig. 12. Combine effect of (a) catalyst dose and pH (b) oxidant dose and pH (c) amount of catalyst and oxidant on RhB degradation.

5. Conclusion

In conclusion, ternary g-C_3N_4/$SrFe_{12}O_{19}$/Zeolite microspheres were created via the hydrothermal method. The ternary heterojunction formed at the interface of $SrFe_{12}O_{19}$ microspheres, zeolite microneedles and g-C_3H_4 sheets helped in charge separation and prevented their recombination hence improving photo efficiency of ternary nanocomposite. The binary and ternary photocatalysts were characterized using a diversity of analytical techniques including FTIR, XRD, SEM-EDS and UV-Vis spectroscopy. When exposed to visible light, the GSZ ternary composite showed excellent photo-activity for breaking down RhB. The whole process was optimized by different parameters such as pH, initial dye concentration oxidant, and catalyst dose and 94% degradation was observed at pH 4, Oxidant dose 10 Mm, catalyst amount 40 mg/100 mL, dye concentration 10ppm, and irradiation time 90 minutes. The catalyst was found to be stable during the reusability study up to five consecutive cycles.

Acknowledgments

The authors would like to acknowledge Deanship of Graduate Studies and Scientific Research, Taif University for funding this work.

References

[1] A.P. Periyasamy, Sustainability 16 495(2024); https://doi.org/10.3390/su16020495
[2] D. Friedmann, Applied Catalysis A: General 649 118943(2023); https://doi.org/10.1016/j.apcata.2022.118943
[3] F. Deng, E. Brillas, Separation and Purification Technology 123764(2023); https://doi.org/10.1016/j.seppur.2023.123764
[4] V.K. Mukkera, S. Katuri, Innovative Trends in Hydrological and Environmental Systems: Select Proceedings of ITHES 2021 821-835(2022); https://doi.org/10.1007/978-981-19-0304-5_57
[5] A. Hareendran, E. Dais, D. Shinoy, S. Srikripa, G.M. Shibu, M. Kurian, Journal of Physics and Chemistry of Solids 161 110398(2022); https://doi.org/10.1016/j.jpcs.2021.110398
[6] H.B. Slama, A. Chenari Bouket, Z. Pourhassan, F.N. Alenezi, A. Silini, H. Cherif-Silini, T. Oszako, L. Luptakova, P. Golińska, L. Belbahri, Applied Sciences 11 6255(2021); https://doi.org/10.3390/app11146255
[7] H.R. Dihom, M.M. Al-Shaibani, R.M.S.R. Mohamed, A.A. Al-Gheethi, A. Sharma, M.H.B. Khamidun, Journal of Water Process Engineering 47 102705(2022); https://doi.org/10.1016/j.jwpe.2022.102705
[8] I. Shakir, P.O. Agboola, S. Haider, Ceramics International 47 28367-28376(2021); https://doi.org/10.1016/j.ceramint.2021.06.254
[9] S.A. Jadhav, H.B. Garud, A.H. Patil, G.D. Patil, C.R. Patil, T.D. Dongale, P.S. Patil, Colloid and Interface Science Communications 30 100181(2019); https://doi.org/10.1016/j.colcom.2019.100181
[10] M. Sarker, S. Shin, J.H. Jeong, S.H. Jhung, Chemical Engineering Journal 371 252-259(2019); https://doi.org/10.1016/j.cej.2019.04.039
[11] I. Ihsanullah, M. Sajid, M. Kabeer, A.M. Shemsi, M.A. Atieh, Water, Air, & Soil Pollution 231 119(2020); https://doi.org/10.1007/s11270-020-04485-2
[12] T. N Lotha, V. Sorhie, P. Bharali, L. Jamir, ChemistrySelect 9 e202304093(2024); https://doi.org/10.1002/slct.202304093
[13] Z. Qi, Z. An, B. Huang, M. Wu, Q. Wu, D. Jiang, Organic & Biomolecular Chemistry 21 6419-6423(2023); 10.1039/D3OB00882G
[14] J.Y. Lu, Z.Q. Bu, Y.Q. Lei, D. Wang, B. He, J. Wang, W.T. Huang, Journal of Molecular Liquids 409 125503(2024); https://doi.org/10.1016/j.molliq.2024.125503
[15] L. Wang, J. Jin, W. Li, C. Li, L. Zhu, Z. Zhou, L. Zhang, X. Zhang, L. Yuan, Energy & Environmental Science 17 9122-9133(2024); 10.1039/D4EE02671C
[16] S. Cui, Y. Liu, X. Dong, X. Fan, Nanomaterials 15 833(2025); https://doi.org/10.3390/nano15110833
[17] J. Liu, B. Wang, J. Huang, R. Yang, R. Wang, Y. Song, C. Wang, Y. Hua, H. Xu, H. Li, Colloids and Surfaces A: Physicochemical and Engineering Aspects 629 127360(2021); https://doi.org/10.1016/j.colsurfa.2021.127360
[18] P. Zhu, M. Hu, M. Duan, L. Xie, M. Zhao, Journal of Alloys and Compounds 840 155714(2020); https://doi.org/10.1016/j.jallcom.2020.155714
[19] M. Ishfaq, A. Aziz, S. Aldaghfag, S. Noreen, M. Zahid, M. Yaseen, Chalcogenide Letters 21 615-629(2024); https://doi.org/10.15251/CL.2024.218.615
[20] H. Shafique, S. Aldaghfag, M. Kashif, M. Zahid, M. Yaseen, J. Iqbal, R. Neffati, Chalcogenide Letters 18 (2021); https://doi.org/10.15251/CL.2021.1810.589
[21] Y. Li, J. Bu, Y. Sun, Z. Huang, X. Zhu, S. Li, P. Chen, Y. Tang, G. He, S. Zhong, Separation and Purification Technology 356 129945(2025); https://doi.org/10.1016/j.seppur.2024.129945
[22] L. Ma, L. Han, S. Chen, J. Hu, L. Chang, W. Bao, J. Wang, Fuel Processing Technology 189 39-48(2019); https://doi.org/10.1016/j.fuproc.2019.02.021
[23] M. Dhashanamoorthy, V. Sharma, S. Chacko, International Journal of Pharmaceutical & Biological Archives 10 216-225(2019);
[24] X. Ren, R. Qu, S. Liu, H. Zhao, W. Wu, H. Song, C. Zheng, X. Wu, X. Gao, Aerosol and Air Quality Research 20 1127-1144(2020); https://doi.org/10.4209/aaqr.2019.12.0651

[25] J. Pan, B. Wang, S. Liu, S. Liu, W. Yan, Molecules 30 554(2025); https://doi.org/10.3390/molecules30030554
[26] M. Hong, L. Yu, Y. Wang, J. Zhang, Z. Chen, L. Dong, Q. Zan, R. Li, Chemical Engineering Journal 359 363-372(2019); https://doi.org/10.1016/j.cej.2018.11.087
[27] K. Prakash, S. Karuthapandian, S. Senthilkumar, Materials Chemistry and Physics 221 34-46(2019); https://doi.org/10.1016/j.matchemphys.2018.09.026
[28] M. Mousavi, A. Habibi-Yangjeh, Magnetically retrievable graphitic carbon nitride-based nanocomposites, Synthesis, Characterization, and Applications of Graphitic Carbon Nitride, Elsevier pp. 305-358(2023)
[29] S. Sharma, H. Sharma, R. Sharma, Chemistry of Inorganic Materials 100035(2024); https://doi.org/10.1016/j.cinorg.2024.100035
[30] S.K. Paswan, P. Kumar, R.K. Singh, S.K. Shukla, L. Kumar, Pollutants and water management: resources, strategies and scarcity 273-305(2021); https://doi.org/10.1002/9781119693635.ch11
[31] M. Hassan, G.A. Ashraf, B. Zhang, Y. He, G. Shen, S. Hu, Chemical engineering journal 380 122483(2020); https://doi.org/10.1016/j.cej.2019.122483
[32] D.A. Vinnik, E.A. Trofimov, V.E. Zhivulin, O.V. Zaitseva, D.A. Zherebtsov, A.Y. Starikov, D.P. Sherstyuk, S.A. Gudkova, S.V. Taskaev, Ceramics International 46 9656-9660(2020); https://doi.org/10.1016/j.ceramint.2019.12.232
[33] J. Lakshmikantha, G. Krishnamurthy, R.H. Nayak, M. Pari, N. Ranjitha, N. Naik, Inorganic Chemistry Communications 146 110175(2022); https://doi.org/10.1016/j.inoche.2022.110175
[34] P. Thakur, S. Jangra, F. Wan, B. Ravelo, A. Thakur, Introduction to Spinel Nano-Ferrites, Applications of Spinel Nano-Ferrites in Health, Environmental Sustainability, and Safety, CRC Press pp. 1-12(2025)
[35] Y. Chang, Y. Zhang, C. Meng, S. Liu, H. Chang, Z. Liu, Applied Physics Letters 116 082404(2020); https://doi.org/10.1063/1.5134122
[36] L. Bo, Y. Hu, Z. Zhang, J. Tong, Polyhedron 168 94-100(2019); https://doi.org/10.1016/j.poly.2019.04.036
[37] I. Ilyashenko, S. Savchenko, N. Martemyanov, A. Chukin, A. Ishchenko, I. Weinstein, Optical Materials 160 116735(2025); https://doi.org/10.1016/j.optmat.2025.116735
[38] S. Agren, J. El Haskouri, E. Beyou, M.H.V.J.S. Baouab, Interfaces, 106873(2025); https://doi.org/10.1016/j.surfin.2025.106873
[39] U. Shukla, Journal of Molecular Structure 1322 140454(2025); https://doi.org/10.1016/j.molstruc.2024.140454
[40] W. Yu, X. You, Y. Wu, C. Li, Q. Wang, X. Yang, X. Bian, Y. Lu, Journal of Environmental Chemical Engineering 13 116271(2025); https://doi.org/10.1016/j.jece.2025.116271
[41] A.R. Gollakota, V. Volli, V.S. Munagapati, J.-C. Wen, C.-M. Shu, Journal of Materials Research and Technology 9 15381-15393(2020); https://doi.org/10.1016/j.jmrt.2020.10.070
[42] U. Rajaji, S. Chinnapaiyan, T.-W. Chen, S.-M. Chen, G. Mani, V. Mani, M.A. Ali, F.M. Al-Hemaid, M.S. El-Shikh, Electrochimica Acta 371 137756(2021); https://doi.org/10.1016/j.electacta.2021.137756
[43] N. Yasmin, M.Z. Iqbal, M. Zahid, S.F. Gillani, M.N. Ashiq, I. Inam, S. Abdulsatar, M. Safdar, M. Mirza, Ceramics International 45 462-467(2019); https://doi.org/10.1016/j.ceramint.2018.09.190
[44] B. Wang, L. Ma, L. Han, Y. Feng, J. Hu, W. Xie, W. Bao, L. Chang, Z. Huang, J. Wang, Chemical Engineering Science: X 10 100089(2021); https://doi.org/10.1016/j.cesx.2021.100089
[45] I. Aslam, M.H. Farooq, U. Ghani, M. Rizwan, G. Nabi, W. Shahzad, R. Boddula, Materials Science for Energy Technologies 2 401-407(2019); https://doi.org/10.1016/j.mset.2019.04.008
[46] M. Laayati, A. Hasnaoui, N. Abdallah, S. Oubaassine, L. Fkhar, O. Mounkachi, S. El Houssame, M. Ait Ali, L. El Firdoussi, Journal of Chemistry 2020 7960648(2020); https://doi.org/10.1155/2020/7960648
[47] N. Tahir, M. Zahid, A. Jillani, S. Tahir, M. Yaseen, Q. Abbas, R.A. Shakoor, S.Z. Hussain, I. Shahid, Journal of Environmental Management 337 117706(2023); https://doi.org/10.1016/j.jenvman.2023.117706

[48] N. Tahir, M. Zahid, A. Jillani, M. Yaseen, Q. Abbas, Journal of Photochemistry and Photobiology A: Chemistry 436 114376(2023); https://doi.org/10.1016/j.jphotochem.2022.114376
[49] N. Nadeem, M. Zahid, A. Tabasum, A. Mansha, A. Jilani, I.A. Bhatti, H.N. Bhatti, Materials Research Express 7 015519(2020); https://doi.org/10.1088/2053-1591/ab66ee
[50] A. Fatima, N. Nadeem, B. Saleh, Z. Rehan, S. Noreen, H.T. Ali, M.J.C.L. Zahid, Chalcogenide Letters 21 895-915(2024); https://doi.org/10.15251/CL.2024.2111.895
[51] C. Wu, S. Huang, X. Cao, Z. Huang, Y. Zhang, Z. Huang, H. Hu, T. Gan, Journal of Environmental Management 389 126147(2025); https://doi.org/10.1016/j.jenvman.2025.126147